Numerical investigation of the coupling of vibrational nonequilibrium and turbulent mixing using state-specific description

Romain Fiévet,[1,*] Stephen Voelkel,[2] Venkat Raman,[1] and Philip L. Varghese[3]
[1]*Department of Aerospace Engineering, University of Michigan, Ann Arbor, Michigan 48109, USA*
[2]*Los Alamos National Laboratory, Los Alamos, New Mexico 87545, USA*
[3]*Institute for Computational Engineering and Sciences, The University of Texas at Austin, Austin, Texas 78712, USA*

(Received 13 July 2018; published 8 January 2019; corrected 25 January 2019)

In flows where the relaxation rate of molecular vibrational energy to equilibrium is comparable to the flow through timescales, the presence of turbulence can alter the mixing and equilibration processes. To understand the coupling between mixing and vibrational relaxation, a novel state-specific species model is solved in a background turbulent flow. The method is applied to mixing of two nitrogen streams at different static temperatures. The relaxation rates for each state are computed using quasiclassical trajectory analysis. The rates obtained from this study were used to first study relaxation to equilibrium in a constant volume bath. Results indicate that the thermal relaxation process is not linear over the range of conditions tested and exhibits quasisteady behavior with the higher energy levels relaxing first, followed by a slower relaxation of the lower energy levels. The state-specific model is then used to study the interaction of turbulent mixing and relaxation process in a turbulent mixing layer of two nitrogen streams at different static temperatures. The direct numerical simulation shows that gas compressibility effects impact the translational energy through flow acceleration and deceleration while the vibrational energy remains constant, triggering vibrational nonequilibrium. Also, the vibrational state populations are significantly affected by turbulence. In certain locations in the jet, the population from the direct calculation is several orders of magnitude different than that based on a Boltzmann distribution at the local vibrational temperature. These results show that considering details of the molecular populations in different vibrational states is important in a range of high enthalpy flows.

DOI: 10.1103/PhysRevFluids.4.013401

I. INTRODUCTION

In high-speed flows, the presence of shocks and expansion waves can alter the partition of internal energies of molecules [1,2], leading to nonequilibrium flow phenomena. While different types of nonequilibrium can be induced due to changes in the different components of thermodynamic internal energy (translational, rotational, vibrational motions), the focus here is on vibrational nonequilibrium. In both internal and external flows of relevance to hypersonic vehicles, the translational and rotational motions are equilibrated quickly as compared to flow timescales. Notably, the presence of slowly equilibrating nitrogen molecules can lead to persistent vibrational

*rfievet@umich.edu

 ©2019 American Physical Society

nonequilibrium [3–5]. While nitrogen itself may be chemically inert at these conditions, the repartition of internal energy can alter turbulence [6,7], shock structures [3,8], or other chemical reactions by altering the energy partition for the reacting molecules [9].

The impact of vibrational nonequilibrium on mixing and chemical reaction rates has been extensively studied and modeled [5,9–12]. While many different models are available [1], the multitemperature approach is often preferred due to its computational ease. This approach assumes that the different molecular motions exhibit a motion-specific equilibrium, leading to a Boltzmann distribution of energies that is characterized by a particular temperature. For instance, when vibrational nonequilibrium is considered, a single translational or rotational temperature and a vibrational temperature per polyatomic species are used to describe the nonequilibrium evolution. These models have been used to study configurations of interest exhibiting strong levels of nonequilibrium, typically high-speed shock-containing flows, such as the supersonic combustion ramjet (scramjet) [4,7,13,14]. Fiévet *et al.* [4] showed that vibrational nonequilibrium can drastically affect ignition time in a scramjet engine. In particular, its effect is counterintuitive. Chemical reaction rates that account for nonequilibrium in external flow often show a decrease in the rate with a reduction in the vibrational component of internal energy. However, for a constant total energy, this reduction is balanced by increased translational energy. Fiévet *et al.* [4] used reaction rates derived from first-principles to demonstrate that the increase in translational energy more than offsets the reduction of vibrational energy, leading to faster ignition times in nonequilibrium flows. While the importance of nonequilibrium is well-known in the context of external hypersonic flows [8], these recent results indicate that nonequilibrium physics could also have a first-order effect in high-speed internal flows, particularly in the context of hypersonic propulsion.

Given the importance of vibrational nonequilibrium effects on these flows, especially in external flows, other higher-order models have been developed to better quantify the energy relaxation process [15–19]. These approaches permit one to describe non-Boltzmann distributions by directly solving for the population in each energy state using detailed rate expressions for the transfer of molecules between the states through collisions. Previous studies of post-shock nonequilibrium using state-specific rates [15,17,18] showed that a Landau-Teller-based multitemperature model was able to approximate the bulk energy exchange process at lower translational temperatures but showed considerable differences at higher temperatures. Further, the relaxation process is not uniformly linear (as assumed by the Landau-Teller models) but can involve quasisteady states [17,18]. Additionally, since chemical reactions have been shown to depend on the vibrational quantum numbers of the reactants, a state-specific approach proved to offer a better estimation of reaction rates [16,17,19]. Multitemperature models were shown to underestimate the dissociation rates as the assumption of a Boltzmann distribution resulted in an underestimation of the high-lying vibrational states populations. However, the main challenge in using such state-specific models is the development of the appropriate state-specific transition rates. Recently, quasiclassical trajectory (QCT) approaches have been used to obtain these rates for select transitions [17,18,20–22]. The focus of all these studies have been on nonturbulent flows.

The current study aims at investigating a nonequilibrium turbulent flow by means of a direct numerical simulation (DNS), where all turbulent scales are resolved, coupled with a vibrational state distribution solver. The solver carries a set of scalars corresponding to the number fractions of vibrational states relevant to the temperature range throughout the computational domain. The simulations will focus on a nonreacting single-species free shear flow where translational and rotational modes are assumed to be in thermodynamic equilibrium, i.e., their state distributions follow a Boltzmann distribution computed from the same temperature. This is a reasonable assumption as these modes reach equilibrium within orders of magnitude fewer collisions than the vibrational mode [2]. Most studies previously cited [4,5,7,10–14] use a multitemperature approach to describe vibrational nonequilibrium: The vibrational state distribution is considered to remain Boltzmann at a different temperature than the translational temperature. This relies on the assumption that the relaxation timescales are identical for all energy states. However, as the vibrational quantum number increases, the state-to-state energy difference decreases, resulting in a much faster relaxation process

at higher energy levels, effectively distorting the distribution from its original Boltzmann shape. This error grows as higher vibrational energy levels are populated for hotter flows, and can lead to erroneous estimation of reaction rates and translational temperature. This last point is crucial in determining the local gas kinetic viscosity, and therefore accurately resolving turbulence structures. In an effort to capture the complexity of the vibrational relaxation process through molecular inelastic collisions, a quasiclassical trajectory model is used to calculate state-specific population rates. This allows the description of non-Boltzmann distribution throughout the flow.

The paper is organized as follows: the first section presents the conservation equations for the single-species compressible flow solver with state-specific vibrational relaxation rates. Then, the derivation of these rates using the QCT approach is detailed for N_2 molecules. The third section presents the application of the QCT-derived rates to resolve 0-D thermal baths. Finally, the state-specific compressible flow solver is used to study a N_2 turbulent jet with vibrational nonequilibrium by the mean of DNS. In the rest of the manuscript, "equilibrium and nonequilibrium" will simply refer to "vibrational equilibrium and nonequilibrium."

II. COMPRESSIBLE FLOW SOLVER WITH VIBRATIONAL STATE-SPECIFIC RELAXATION RATES

In this section, the details of the state-specific nonequilibrium description are provided.

A. Conservation equations for thermally perfect gas

In this work, all simulations are carried out using N_2 as the fluid. To begin with, the conservation equations that describe thermally perfect equilibrium gas are written as

$$\frac{\partial \rho}{\partial t} + \frac{\partial \rho u_i}{\partial x_i} = 0, \tag{1}$$

$$\frac{\partial \rho u_i}{\partial t} + \frac{\partial \rho u_i u_j}{\partial x_j} = -\frac{\partial P}{\partial x_i} + \frac{\partial \tau_{ij}}{\partial x_j}, \tag{2}$$

$$\frac{\partial \rho E}{\partial t} + \frac{\partial \rho u_i E}{\partial x_i} = -\frac{\partial P u_i}{\partial x_i} + \frac{\partial \tau_{ij} u_j}{\partial x_i} - \frac{\partial q}{\partial x_i}, \tag{3}$$

where ρ is the mass density of the fluid, u_i the ith velocity component, P is the static pressure, τ_{ij} is the surface shear stress tensor, $E = e + \frac{1}{2}u_i u_i$ is the total energy, e is the mass-specific internal energy, and q is the heat diffusion rate. Also, t and x_i represent time spatial coordinates, respectively. The specific heat capacity used to compute the internal energy is based on a ninth-order polynomial function [23]. The shear stress components τ_{ij} are defined assuming the flow is a Newtonian fluid, so that

$$\tau_{ij} = \mu\left(\frac{\partial u_i}{\partial x_j} + \frac{\partial u_j}{\partial x_i} - \frac{2}{3}\delta_{ij}\frac{\partial u_k}{\partial x_k}\right), \tag{4}$$

where the kinetic viscosity μ is evaluated using Sutherland's law and is a function of the flow translational temperature T, and δ is the Kronecker operator. The heat diffusion rate is defined assuming Fourier's law, so that

$$q = -\lambda\frac{\partial T}{\partial x_i}, \tag{5}$$

where λ is the thermal conductivity calculated from the Prandtl number Pr, which relates heat and momentum diffusion. A constant $Pr = 0.72$ is used in this study.

B. Modifications to resolve vibrational state-specific nonequilibrium

To resolve vibrational nonequilibrium, it is necessary to split the total energy conservation equation into its different modes. There are many levels of description possible. Two different approaches will be used in this work. In both descriptions it is assumed that the translational and rotational modes are in equilibrium and only the vibrational mode is out of equilibrium. Given a molecular population, the internal energy in the vibrational mode is the sum of the internal energies of the individual molecules. From an energy balance perspective, the internal energy is split into molecular vibrational energy, e_v, translational energy e_t, and rotational energy e_r. As a first approximation, the distribution of energies in each mode is assumed to follow the Boltzmann function with a corresponding temperature. The vibrational temperature is denoted by T_v, while a single temperature is used for the translational and rotational modes (denoted simply by T from henceforth). For a diatomic molecule such as N_2, e_v and T_v form a bijection, which for this work is given by

$$e_v(T_v) = e(T_v) - e_{\text{tr}}(T_v) \tag{6}$$

$$= \int_{T_{\text{ref}}}^{T_v} c_v(T')dT' - \frac{5}{2}R(T_v - T_{\text{ref}}), \tag{7}$$

where $e_{\text{tr}} = e_t + e_r$ is the ro-translational energy, $T_{\text{ref}} = 298.15$ K is a reference temperature, R is the gas constant, and c_v is the gas specific heat at constant volume. Note that in this formulation, e_v equals 0 at T_{ref} and therefore does not account for the ground-state vibrational energy, which is naturally included in the c_v relation.

Decomposing the total energy relation defined in Eq. (3), the transport relations for the kinetic-translational-rotational energy, denoted $e_{\text{trk}} = e_t + e_r + \frac{1}{2}u_i u_i$, and the vibrational energy are given by

$$\frac{\partial \rho e_{\text{trk}}}{\partial t} + \frac{\partial u_j(\rho e_{\text{trk}} + P)}{\partial x_j} = \frac{\partial}{\partial x_j}\left(\lambda \frac{\partial T}{\partial x_j}\right) - \frac{\partial}{\partial x_j}(\tau_{ij}u_i) + Q_{\text{TR-V}}, \tag{8}$$

$$\frac{d\rho e_v}{dt} + \frac{\partial \rho u_j e_v}{\partial x_j} = \frac{\partial}{\partial x_j}\left(\lambda_v \frac{\partial T_v}{\partial x_j}\right) - Q_{\text{TR-V}}, \tag{9}$$

where $Q_{\text{TR-V}}$ is the energy exchange rate between the internal translational-rotational and vibrational energy modes, and λ_v is the vibrational conductivity. To be consistent with Eq. (3), the vibrational conductivity is defined as

$$\lambda_v = \frac{\mu c_{p,v}}{\text{Pr}}. \tag{10}$$

In this work, the Prandtl number is assumed to be identical for all internal energy modes. The $Q_{\text{TR-V}}$ energy exchange rate can be evaluated using Landau-Teller model with Millikan and White relaxation timescales [2,3,7,24].

By using a single temperature to describe the vibrational energy, the multitemperature model has made a fundamental assumption: The distribution of vibrational energy among the molecules is governed by a Boltzmann distribution, albeit with the vibrational temperature T_v that is different from the translational temperature. As previously explained, this assumption is unlikely to be valid for high enthalpy flows, and could introduce errors in the estimation of chemical reaction rates even for lower enthalpy flows. A more detailed approach is to directly solve for the population density in individual vibrational states. This is equivalent to solving the master equation for spatially extended systems.

When using the state-specific approach, Eqs. (1), (2), (3), and (8) are still used. However, Eq. (9) is further decomposed into a set of transport equations for the fractional number densities that describe the populations of molecules in individual vibrational energy levels, denoted by ϕ_v for vibrational state v. That is, for a particular vibrational state v, the number density n_v is the number

of particles per unit volume at that state (units of $1/m^3$), and $\phi_v = n_v/n$, where $n = \sum_v n_v$. Note that ϕ_v is dimensionless and $\sum_v \phi_v = 1$. Furthermore, considering that $nm_{N_2} = \rho$, where m_{N_2} is the mass of one molecule, then $\rho\phi_v$ represents the mass of all the particles with vibrational quantum number v per unit volume (units of kg/m^3). Next, note that the state-averaged vibrational energy is defined as

$$e_v = \sum_v \frac{\varepsilon_v(v) - \varepsilon_v(0)}{\rho} n_v = \sum_v \frac{\varepsilon_v(v) - \varepsilon_v(0)}{\rho} n\phi_v = \sum_v \frac{\varepsilon_v(v) - \varepsilon_v(0)}{m_{N_2}} \phi_v, \tag{11}$$

where $\varepsilon_v(v)$ is the quantized vibrational energy of a molecule in vibrational state v. Hence, transporting all the states number fractions permits one to calculate the gas vibrational energy and replace Eq. (9). The transport equation for fractional density ϕ_v can be written as

$$\frac{\partial \rho\phi_v}{\partial t} + \frac{\partial \rho u_i \phi_v}{\partial x_i} = \frac{\partial}{\partial x_i} \rho D \frac{\partial \phi_v}{\partial x_i} + \dot{S}_v, \tag{12}$$

where the mass diffusion rate ρD is evaluated using a Schmidt number Sc equal to 0.72, such that $\rho D = \frac{\mu}{Sc}$. $\dot{S}_v$ is the vth number fraction source term. This source term is calculated from the state-specific inelastic scattering rates of the following collision process:

$$N_2(v_1) + N_2(v_2) \longrightarrow N_2(v_1') + N_2(v_2'). \tag{13}$$

The inelastic collisions, which result in a change of vibrational quantum numbers, evolve the states fraction numbers through time. As such, every ϕ_v can be considered as a distinct species and the inelastic collisions as reaction rates. This analogy permits us to evaluate $\dot{S}_v$ using a law of mass action for every collision as

$$\dot{S}_v = \sum_i \sum_j \sum_k \sum_l g_{v,ijkl} \frac{k_s(v_i \to v_k, v_j \to v_l, T)}{M_{N_2}} (\rho\phi_i)(\rho\phi_j), \tag{14}$$

where M_{N_2} is the molar mass (units of kg/mol), $g_{v,ijkl}$ is a degeneracy factor which characterizes the impact a particular reaction would have on the mth population level. Here, $g_{v,ijkl}$ is defined as

$$g_{v,ijkl} = -\delta_{i,v} - \delta_{j,v} + \delta_{k,v} + \delta_{l,v}. \tag{15}$$

Here, these scattering rates k_s are calculated using a QCT approach which will be presented in detail in the following section.

In the multitemperature model, the coupling between Eqs. (8) and (9) occurred through the energy exchange term Q_{TR-V}. In the state-specific approach, Q_{TR-V} can be calculated from all the scattering rates k_s which naturally account for the energy exchange between translational+rotational and vibrational modes. For instance, the k_s rate for reaction $(v_1 = 1, v_2 = 1)$ to $(v_1' = 1, v_2' = 2)$ characterizes a transfer of energy from the translational and rotational modes to the vibrational mode, hence a negative Q_{TR-V}. Likewise, $(v_1 = 1, v_2 = 2)$ to $(v_1' = 1, v_2' = 1)$ corresponds to a positive Q_{TR-V}. Therefore, Q_{TR-V} is calculated in the state-specific approach as

$$Q_{TR-V} = -\sum_v \frac{\varepsilon_v(v) - \varepsilon_v(0)}{m_{N_2}} \dot{S}_v. \tag{16}$$

III. DERIVATION OF STATE-SPECIFIC VIBRATIONAL RELAXATION RATES

A. QCT formulation of inelastic rates

The vibrational inelastic rates k_s for the reaction presented in Eq. (13) were calculated using QCT analysis [9,20,21,25,26]. The potential energy surface (PES) utilized for these calculations was developed by Bender *et al.* [20], which was an extension of the surface developed by Paukku *et al.* [27]. This analytic PES was accessed via an online potential energy surface library, POTLIB [28]. As detailed by the developers, the PES was fit using a set of approximately 17,000 *ab initio*

data points [20]. The reported root-mean-square error compared to the quantum calculations is 1.3 kcal/mol for energies less than 100 kcal/mol and 6.7 kcal/mol for all data points on the surface.

We note here that this PES was not originally intended for predicting modest temperature scattering processes as those of interest in this work. Instead, the PES was developed with the purpose of studying nitrogen dissociation at earth reentry conditions. At higher temperatures, direct molecular simulations (DMS) have shown reasonable agreement compared to Millikan and White [29]. However, no formal validation of the vibrational exchange rates has been performed for this surface for temperatures at and below 4 000 K.

Here, the rates were determined as a function of a translational-rotational temperature T, an initial set of vibrational quantum numbers $\boldsymbol{v} = (v_1, v_2)$, and a final set of vibrational numbers $\boldsymbol{v}' = (v_1', v_2')$. The scattering rate is denoted as $k_s(\boldsymbol{v}, \boldsymbol{v}', T)$. For each trajectory, $\boldsymbol{v}$ is fixed, and the relative speed and initial rotational quantum numbers, $\boldsymbol{J} = (J_1, J_2)$, are sampled from their respective probability distribution functions (PDFs). Since the rotational and translational motions are assumed to be at equilibrium, these PDFs represent the Boltzmann and Maxwell distributions, respectively. After the N_2 molecules collide, the final state is marked (i.e., $\boldsymbol{v}'$) based on the closest state. The aggregation of the outcomes is used to determine the inelastic scattering rates. The following section describes the process used in calculating k_s for the N_2-N_2 system.

Following conventional QCT averaging methods, which utilize Monte Carlo integration to approximate the integrals associated with sampling the phase space of the system [30], the scattering probability P_s is approximated by

$$P_s(\boldsymbol{v} \to \boldsymbol{v}', \boldsymbol{J} \to \boldsymbol{J}', g, b) \approx \frac{N_s(\boldsymbol{v}', \boldsymbol{J}')}{N(\boldsymbol{v}, \boldsymbol{J}, g, b)}. \tag{17}$$

where g is the relative speed of the reactants, b is the impact parameter, N is the number of trajectories sampled at fixed $(\boldsymbol{v}, \boldsymbol{J}, g, b)$ with all other initial conditions sampled from there respective PDFs, and N_s denotes the number of trajectories with a post-collision rovibrational quantum numbers $(\boldsymbol{v}', \boldsymbol{J}')$. The relative uncertainty of P_s, denoted by $\mathcal{U}_s$, is defined in this work as two standard deviations normalized by P_s (this corresponds to a 95% confidence interval), which is given by [9,20,25,26]

$$\mathcal{U}_s = 2\left(\frac{1}{N_s} - \frac{1}{N}\right)^{1/2} \approx 2\left(\frac{1}{N_s}\right)^{1/2}, \tag{18}$$

where dependencies were dropped for brevity and the approximation is valid when $N \gg N_s$. So, for a 95% confidence interval to be within 5% of the mean (i.e., $\mathcal{U}_s = 0.05$), approximately 1600 trajectories in which $\boldsymbol{v} \to \boldsymbol{v}'$ need to be observed.

If the rotational state, relative speed, and impact parameter are also sampled from their respective PDFs as initial conditions, then the transition rate from one vibrational state to another for a fixed temperature is approximated by

$$k_s(\boldsymbol{v} \to \boldsymbol{v}', T) \approx \pi b_{\max}^2 \left(\frac{8 k_B T}{\pi m_r}\right)^{1/2} \frac{N_s(\boldsymbol{v}')}{N(\boldsymbol{v})}, \tag{19}$$

where $P_s = 0$ for all $b > b_{\max}$, m_r is the reduced mass of the reactants, and k_B is the Boltzmann constant. The PDFs for b, g, and J_i are, respectively, defined as

$$f_b = 2\pi b, \tag{20}$$

$$f_g(g; T) = \left(\frac{m_r}{2\pi k_B T}\right)^{3/2} 4\pi g^2 e^{-m_r g^2/2k_B T}, \tag{21}$$

$$f_{r,i}(J_i; v_i, T) = \frac{g_s(J_i)(2J_i + 1) e^{-\frac{\epsilon_{int}(v_i, J_i) - \epsilon_{\text{int}}(v_i, 0)}{k_B T}}}{Q_{r,i}(v_i, T)}, \tag{22}$$

where g_s is the spin degeneracy of the rotational state, ϵ_{int} is the internal energy, and Q_r is the rotational partition function, which normalizes $f_{r,i}$. The combined rotational PDF is denoted $f_r(\boldsymbol{J}; \boldsymbol{v}, T) = f_{r,1}(J_1; v_1, T) f_{r,2}(J_2; v_2, T)$.

The rates as defined in Eq. (19) are completely independent of one another. Thus, the QCT-calculated rates are not necessarily symmetric and detailed balance at thermal equilibrium is not guaranteed. To ensure that the rates are consistent (i.e., the rates are symmetric and satisfy detailed balance), the rates are averaged accordingly. First, for symmetry, the rates are modified so that

$$k_s[(v_1, v_2) \rightarrow (v_1', v_2')] = k_s[(v_2, v_1) \rightarrow (v_2', v_1')] \tag{23}$$

This relation is imposed directly in Eq. (19) by setting

$$N(\boldsymbol{v}) = N(v_1, v_2) + N(v_2, v_1) \tag{24}$$

$$N_s(\boldsymbol{v} \rightarrow \boldsymbol{v}') = N_s(v_1 \rightarrow v_1', v_2 \rightarrow v_2') + N_s(v_2 \rightarrow v_2', v_1 \rightarrow v_1'). \tag{25}$$

Note that $\boldsymbol{v}$ is added as a dependency for N_s to clarify how final states are counted. Next, for detailed balance, the rates are modified so that

$$f_v(\boldsymbol{v}, T) k_s(\boldsymbol{v} \rightarrow \boldsymbol{v}', T) = f_v(\boldsymbol{v}', T) k_s(\boldsymbol{v}' \rightarrow \boldsymbol{v}, T), \tag{26}$$

where $f_v(v, T)$ is the Boltzmann PDF characterizing vibrational state v's number fraction. The final rate used in the CFD simulations, i.e., the rate inserted into Eq. (14), was chosen as the average of the two rates defined in Eqs. (19) and (26). That is, k_s was is now defined as

$$k_s(\boldsymbol{v} \rightarrow \boldsymbol{v}', T) = \frac{\pi b_{\max}^2}{2} \left(\frac{8 k_B T}{\pi m_r} \right)^{1/2} \left[\frac{N_s(\boldsymbol{v} \rightarrow \boldsymbol{v}')}{N(\boldsymbol{v})} + \frac{f_v(\boldsymbol{v}', T)}{f_v(\boldsymbol{v}, T)} \frac{N_s(\boldsymbol{v}' \rightarrow \boldsymbol{v})}{N(\boldsymbol{v}')} \right], \tag{27}$$

where N and N_s are defined in Eqs. (24) and (25), respectively.

B. State-specific relaxation rates

Inelastic scattering rates were directly calculated using the QCT method as derived in Sec. III at nine translational-rotational temperatures T = [500, 1000, 1500, 2000, 2500, 3000, 4000, 5000, 6000] K.

The first 10 vibrational quantum numbers were sampled, so for N_2-N_2 collisions, there exist 10^4 vibrational state combinations (i.e., degrees of freedom). A total of 2.8×10^9 trajectories were simulated using the QCT program developed by Voelkel *et al.* [9,21,25] on the Texas Advanced Computing Center (TACC) machine using 4104 cores for 30 hours. At the end of each trajectory, the final vibrational quantum number was determined as the closest lying state compared to the classical vibrational energy resulting from the collision.

In total, 9×10^4 rates needed to be calculated based on the sampled states (including both inelastic and elastic collisions). However, many of the final states were never observed, implying that the probability of the particular transition was approximately zero. Table I summarizes the number of trajectories and rates calculated per temperature.

Fewer transitions were observed at lower temperatures (resulting in fewer calculated rates) because the total energy of the colliding N_2-N_2 pair was not sufficient to shift the vibrational state. At high temperatures and vibrational quantum numbers, more energy is stored in translational-rotational and vibrational energy modes on average. This increases the total energy that can be repartitioned during the collision event, which in turn increases the likelihood of observing vibrational transitions.

The sets of directly calculated inelastic rates at 2000 and 4000 K are plotted in Fig. 1, which are referred to as the rate matrix for a particular translational temperature. The x and y axes correspond to the initial/final state of the first and second nitrogen molecule, respectively. Because symmetry was enforced, the rate matrix is symmetric across the $x = y$ diagonal. Note that if the rate is zero,

TABLE I. Number of trajectories and rates calculated per sampled temperature.

Temperature (K)	Trajectories	Calculated rates
500	2.3×10^8	438
1000	2.3×10^8	468
1500	2.3×10^8	480
2000	2.3×10^8	526
2500	1.6×10^7	512
3000	2.3×10^8	877
4000	6.3×10^8	2493
5000	5.0×10^8	4344
6000	5.0×10^8	6124

this implies that the transition was not recorded throughout the QCT simulation. Hence, the rate matrix at 2000 K is sparse because most vibrational state transitions were not observed, whereas the rate matrix at 4000 K is less sparse. Note that the rates at the other temperatures follow the general trends seen for these two temperatures.

In Fig. 1(a), the directly calculated rates for low-lying vibrational states is observed to be zero, but the physical rate is nonzero. This discrepancy is due to the statistical nature of the QCT method and the low probability of observing such a transition. To reduce this statistical error, the scattering rates at low temperatures were extrapolated from the rates at high temperatures. Furthermore, from the set of directly calculated rates, as modified to enforce the detailed balance [Eq. (26)], the scattering rates were also fit to an functional relation. This fit was then tabulated and accessed during the CFD simulations to determine the rate for intermediate temperatures between 2000 and 4000 K. For the interpolation, it was assumed that $\log(k_s) \propto T^{-1}$, similar to the conventional Arrhenius expression. The interpolated (or extrapolated if necessary) rate matrices at 2000 and 4000 K are plotted in Fig. 2. Comparing Fig. 2(b) with Fig. 1(b), notice that the structure of the rate matrix for 4000 K is approximately unchanged. However, at 2000 K, the interpolated rate matrix is significantly less sparse than before. Specifically, the nonzero entries in the rate matrix were increased from 526 to 2521. These interpolated rate matrices are used in the simulations presented in Secs. IV and V.

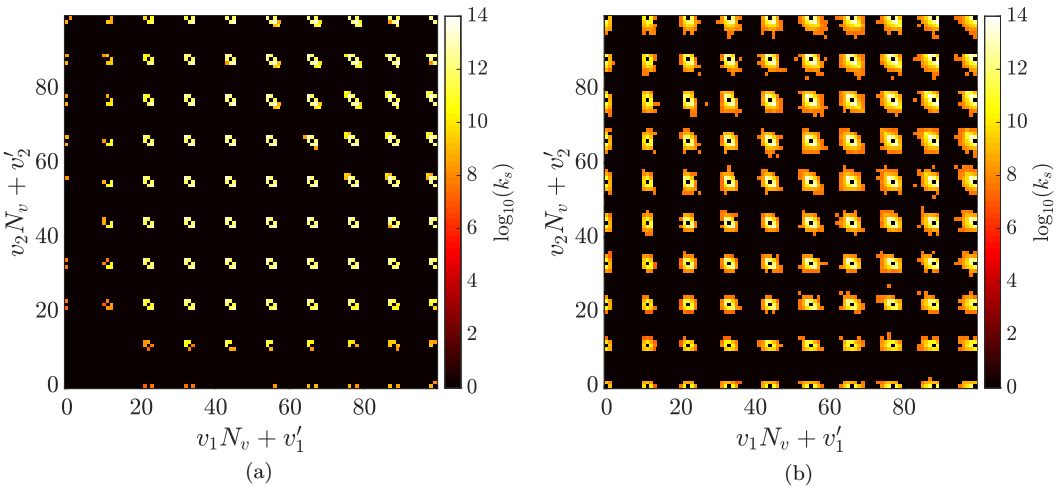

FIG. 1. Directly calculated inelastic scattering rates [units for the rate are $cm^3/(mol\ s)$]: (a) $T = 2000\,K$; (b) $T = 4000\,K$

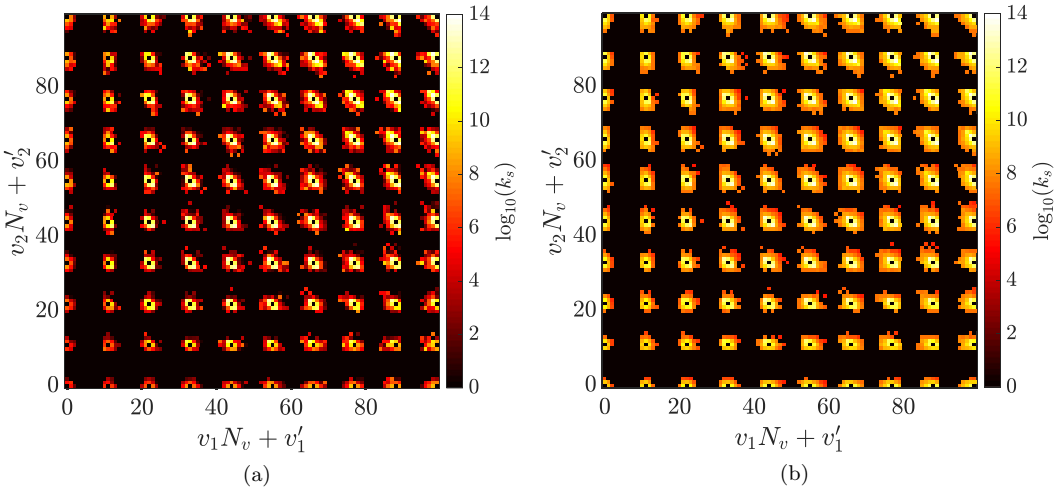

FIG. 2. Interpolated and extrapolated inelastic scattering rates [units for the rate are cm^3/(mol s)]: (a) $T = 2000$ K; (b) $T = 4000$ K.

The relative error of the Arrhenius fit (denoted k_s^a) is shown in Fig. 3.

The points only represent comparisons to those rates which were directly calculated. In general, the high rates have a lower error, which is good because those rates were well resolved. At lower-valued rates, the difference between the fit and the rate is more sporadic. However, the lower rates generally had a higher corresponding uncertainty, thus implying that the directly calculated rates had a larger margin of error. Furthermore, the rates span six orders of magnitude, implying that the relative effect of the lower rates on the simulation will be less impactful.

C. Compact formulation of the state-specific rates

In an effort to reduce the cost of evaluating $\dot{S}_v$ [Eq. (12)] at each time step, the source term is not directly evaluated as a summation over all 10^4 states [Eq. (14)]. Instead, this evaluation is reduced

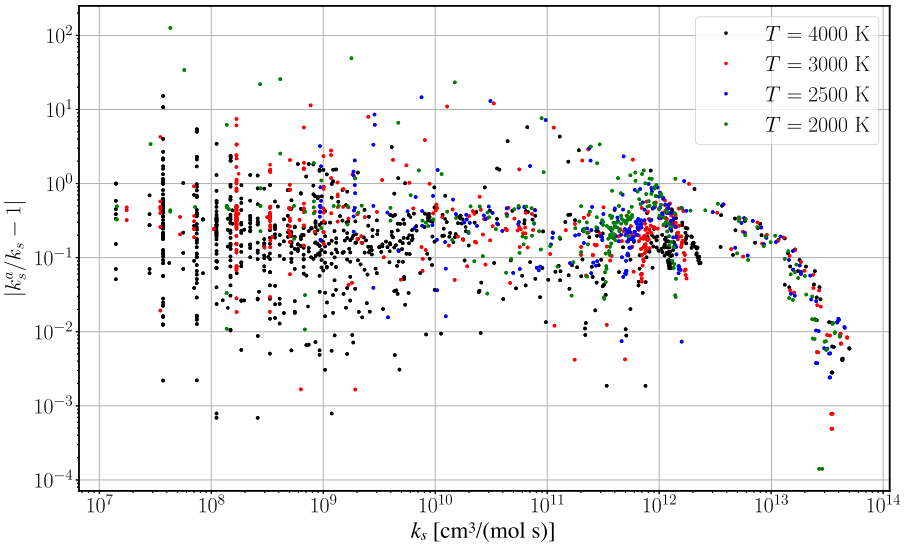

FIG. 3. Relative error of Arrhenius fit rates compared to directly calculated rates.

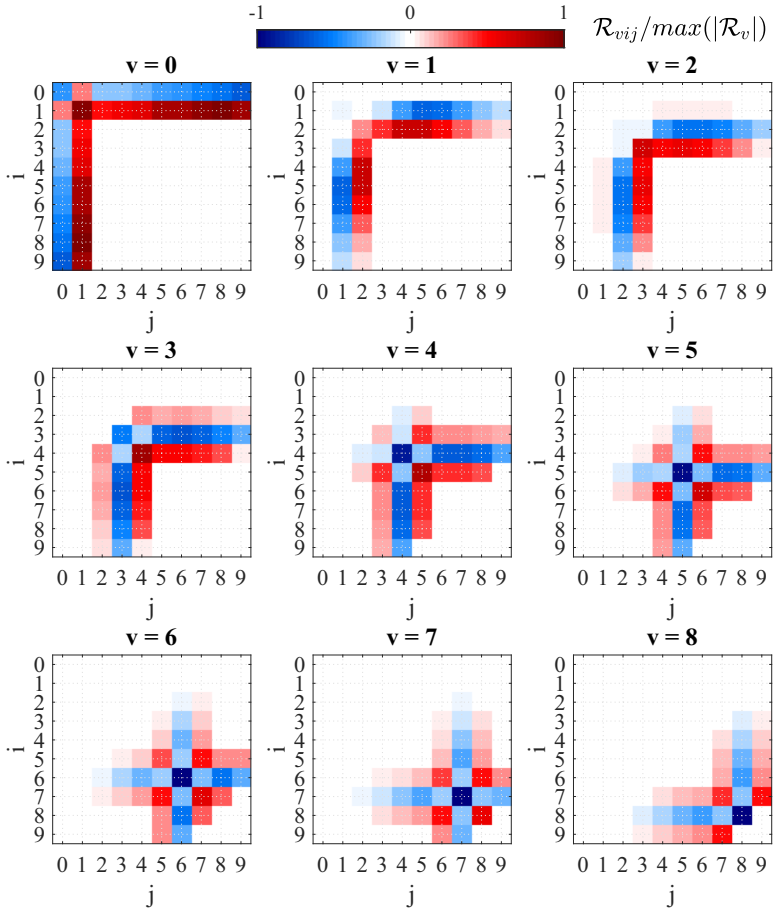

FIG. 4. $\mathcal{R}_{vij}$ for the first 9 levels ($v = [0\ 8]$) normalized by its peak values at a temperature of 4000 K. Dark blue corresponds to a maximum depletion, and dark red to a maximum replenishment of ϕ_v.

into a more compact form during the initialization of the simulation. In Eq. (14), the summations on the index k and l corresponding to the product of the scattering reaction rate can be precomputed into a three-dimensional matrix $\mathcal{R}_{vij}$ of size N_{level}^3, where N_{level} is the number of levels. $\mathcal{R}_{vij}$ defined as

$$\mathcal{R}_{vij} = \sum_k \sum_l g_{v,ijkl} \times \frac{k_s(v_i \rightarrow v_k, v_j \rightarrow v_l, T)}{M_{\text{N}_2}}. \tag{28}$$

Then, Eq. (14) simply becomes

$$\dot{S}_v = \sum_i \sum_j \mathcal{R}_{vij}(\rho\phi_i)(\rho\phi_j). \tag{29}$$

For each vibrational energy level v, $\mathcal{R}_{vij}$ provides information on the addition/depletion of population due to combination of states $\{i, j\}$. Figure 4 presents $\mathcal{R}_{vij}$ for the first 9 levels ($v = [0\ 8]$) at a temperature of 4000 K. Note that the range for each level v is normalized by its peak value $\max(|\mathcal{R}_v|) = [0.648.5470.61239.72401.13915.35262.46474.47467.3] \times 10^6\,\text{kg}\,\text{m}^{-3}\,\text{s}^{-1}$ to better reveal the slow-reacting lower levels contours. Note that the highest level rates are 4 orders of magnitude higher than the ground-state rates. As necessary, the table is symmetric along the $i = j$

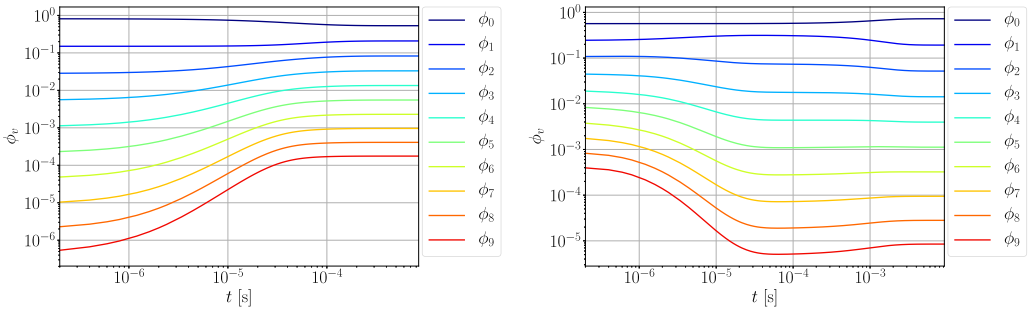

FIG. 5. Vibrational state populations versus time in constant volume for varied initial conditions; (a) $T_v^0 = 2000$ K, $T_0 = 4000$ K; (b) $T_v^0 = 4000$ K, $T_0 = 2000$ K.

diagonal. A first observation is that almost all cells located on the $i = v$ or $j = v$ lines are blue; i.e., collisions involving at least one molecule of level v usually result in a depletion of ϕ_v. At higher levels ($v > 3$), depletion is usually maximum when both colliding molecules are initially at level v. However, peak depletion tends to be shifted towards the right or left of the $(i, j) = (v, v)$ cell for lower levels as inelastic collisions with a molecule is more likely to occur when involving a partner at a higher level. This trend is clearly observed for the $v = 2$ table. At 4000 K, an $(i, j) = (2, 2)$ collision is less effective at depleting ϕ_2 than a $(i, j) = (6, 2)$ collision. Interestingly, the ground-state rates table is characterized by a positive production (red cell) for any neighbor of the $(i, j) = (0, 0)$ cell. Similarly, the highest replenishment rates are found for high levels ($v > 3$) in vicinity of the (v, v) cell on its diagonals. For the temperatures considered here, the fourth quadrant (both $i, j > v$) always have higher rates than the second quadrant (both $i, j < v$).

IV. THERMAL BATH SIMULATIONS

The state-specific rates are first used in a zero-dimensional thermal bath in order to verify the equilibration process. The governing equations for the thermal bath are based on those presented in Sec. II. Specifically, spatial derivatives are neglected in a constant volume system, which results in a set of algebraic relations for mass, momentum, and energy. The vibrational population distribution is then expressed in terms of a set of ordinary differential equations, leading to the following system of equations:

$$\rho(e_{\text{trk}} + e_v) = \rho_0\left(e_{\text{tr}}^0 + e_v^0\right), \tag{30}$$

$$\frac{d}{dt}(\rho\phi_v) = \dot{S}_v, \tag{31}$$

$$\phi_v^0 = f_v(v, T_{v,0}), \tag{32}$$

where 0 subscript or superscript refers to the state at time $t = 0$ (note that mass and momentum are assumed to be automatically satisfied). The initial vibrational state distribution is defined based on a Boltzmann distribution at a chosen vibrational temperature. The translational temperature is independently set, so that the system is out of thermal equilibrium. At the system evolves, the vibrational state distribution will move towards its equilibrium distribution, and the translational temperature as well as the pressure will shift due to the conservation relations.

Two cases were tested: (1) $T_{v,0} < T_0$ (cold to hot), and (2) $T_{v,0} > T_0$ (hot to cold). In both cases, the initial pressure was set to 1 atm. Figure 5 shows one set of simulation results for each of the two cases. For the cold to hot case, the vibrational states are initially defined by a Boltzmann distribution at $T_{v,0} = 2000$ K, whereas the bath is at $T_0 = 4000$ K. Each of the states relax over similar timescales, with the $v = 9$ and $v = 0$ states taking approximately 5×10^{-5} s and 2×10^{-4} s

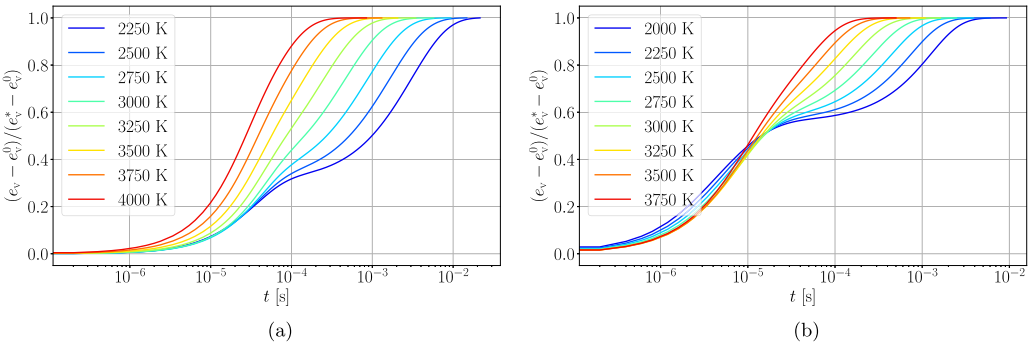

FIG. 6. Vibrational energy versus time in constant volume for varied initial conditions; (a) $T_v^0 = 2000$ K, T_0 varied; (b) $T_v^0 = 4000$ K, T_0 varied.

to relax, respectively. In contrast, the relaxation from hot to cold differs considerably. Here, the vibrational states are initially defined by a Boltzmann distribution at $T_{v,0} = 4000$ K, whereas the bath is at $T_0 = 2000$ K. In this system, the high-lying vibrational states relax by 4×10^{-5} s. At this point, most of the exchanged energy is deposited into the $v = 1$ state. Then, a quasi-steady-state is reached that is sustained until 4×10^{-4} s, after which low lying states relax.

The above cases present two different types of relaxation—the Landau-Teller-type linear relaxation to the end state and the second quasi-steady-state based exchange of energy. It is found that in most other cases, both these types are present. However, when the translational temperature is lower than the initial vibrational temperature, the quasi-steady-state is more pronounced. This is further seen in the plot of vibrational energies shown in Figs. 6(a) and 6(b). For the cold-to-hot case where $T_v^0 = 2000$ K, the higher initial translational temperatures relax uniformly. The lower translational temperatures relax to a near quasi-steady-state. In contrast, for the hot-to-cold case where $T_v^0 = 2000$ K, all of the simulations relax at a similar rate up to 10^{-5} s. After this point, the higher translational temperature simulations continue to relax uniformly, whereas the lower translational temperature simulations reach a quasi-steady-state before relaxing towards equilibrium. Such quasi-steady-states have been observed previously in other studies as well [17,18].

Based on these simulations, a relaxation timescale can be extracted assuming a linear process, and compared with the empirical correlations of Millikan and White [31]. The dependence of these timescales on the translational temperature is plotted in Figure 7. The translational temperature and pressure used is taken as the average of the initial and equilibrium values. The relaxation time τ_v is

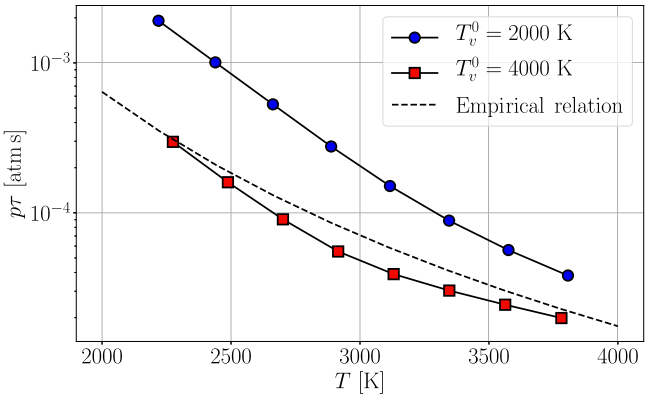

FIG. 7. Vibrational energy relaxation timescales compared to Millikan and White's empirical model [31].

TABLE II. Numerical inflow conditions.

Case	U_{jet} [m/s]	U_{coflow} [m/s]	T_{jet} [K]	T_{coflow} [K]	Bulk $\text{Re}_{H/2}$
1	400	80	2000	4000	3921
2	400	80	4000	2000	1364

defined as the time for the vibrational energy to reach 63.2% of its equilibrium value. It is important to note that the empirical relation assumes that the relaxation timescale is independent of the initial vibrational population distribution. However, simulations performed here showed that the initial conditions have an effect. For instance, when the initial vibrational population is at a higher than equilibrium total energy, the relaxation time is comparable to the correlation value, but the process is considerably slower than predicted by the correlation when the initial vibrational temperature is lower than the translational temperature. Regardless, the dependence on temperature seems to closely follow the $T^{-1/3}$ correlation. These differences have been noted at higher temperatures in other studies as well [18].

V. TURBULENT PLANAR JET SIMULATIONS

The effect of turbulence on nonequilibrium is studied next using a planar jet configuration. This case involves a central jet issuing into a coflow, with both streams composed only of N_2. For this particular calculation, all streams are subsonic but in the compressible regime. Turbulent mixing is expected to trigger vibrational nonequilibrium as observed by Reising *et al.* [32]. For the discussion below, *cold* or *hot* nonequilibrium will refer to a vibrationally under-excited or over-excited flow, respectively.

A. Numerical details

Two direct numerical simulations of N_2-N_2 mixing are conducted. The height of the planar jet is 8 mm, while the spanwise width is 16 mm. The computational domain is 160 mm long, and is discretized using $(n_x, n_y, n_z) = (3072, 960, 196)$ control volumes in the three coordinate directions. The domain is periodic in the spanwise direction, and nonreflective characteristic boundary conditions [33] are applied at all the nonstreamwise boundaries of the domain. The inflow conditions for the central jet are obtained from an auxiliary simulation of a periodic turbulent channel flow. This fully developed solution is sampled to generate an inflow file that is used to impose a time-varying but correlated inflow condition. Both the jet and the coflow are specified to be at a static pressure of 2 atm, and are assumed to be in thermal equilibrium. The two cases use different static temperatures for the two streams to reproduce hot-to-cold and cold-to-hot mixing of the vibrational population. The other inflow conditions for the two cases are provided in Table II.

The simulations were performed using the state-specific nonequilibrium flow approach. The numerical solver uses a finite difference fifth-order WENO LLF scheme with characteristics reconstruction to compute the convective fluxes [34], while a fourth-order central scheme is used for the diffusion terms. Time-integration is carried out using a fourth-order Runge-Kutta scheme. Other details of the flow solver are provided in Koo [35]. The dynamic viscosity is determined using Sutherland's law, but was increased by a factor of 4 in order to provide DNS-like resolution. The simulations were initially conducted until all initial condition related effects have been convected out of the domain. Statistics were then sampled over 0.25 ms, which corresponds to 0.5 flow-through times, evaluated based on the integrated centerline velocity. A Courant-Friedrichs-Lewy condition of 0.9 was used, leading to time-step of 80 ns. The code uses domain-decomposition based parallelization, and each simulation was run on 10 000 cores for 16 h. An inert mixture fraction Z_{mix} was transported along with the populations for the 10 vibrational states. Mixture

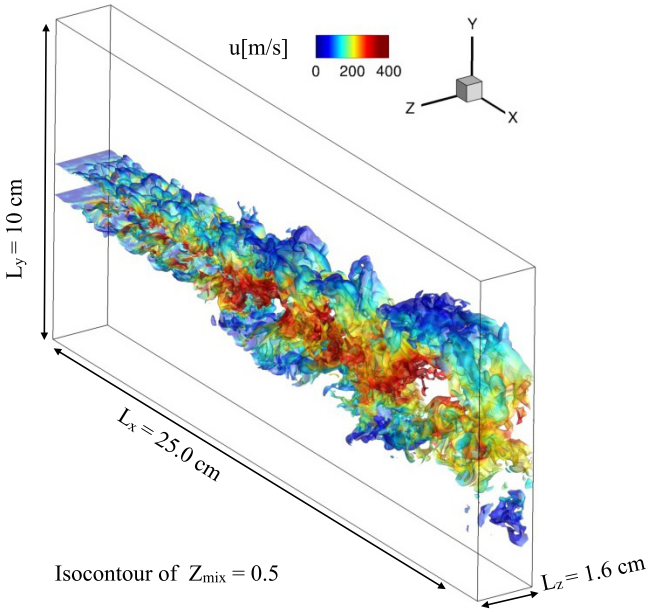

FIG. 8. Isocontour of mixture fraction $Z_{\text{mix}} = 0.5$ colored by streamwise velocity.

fraction is widely used in combustion studies to quantify the interplay between chemical reactions and turbulent mixing [36]. In these simulations, mixture fraction is set to 1 for the jet inflow, and 0 for the coflow. The computational domain and a snapshot of the mixing layer are shown in Fig. 8.

Figure 9 presents an instantaneous snapshot of the density gradient magnitude, indicating a highly turbulent mixing layer. It is seen that the potential core of the jet extended until $x/H \approx 7.5$. To ensure that the turbulence length-scales are adequately captured, the local grid size is compared to the Kolmogorov length scale κ defined as $\kappa = \nu^{\frac{3}{4}}\epsilon^{-\frac{1}{4}}$ where the turbulent dissipation rate ϵ is defined as $\epsilon = \frac{1}{\rho}\overline{\tau_{ij}\frac{\partial u_i'}{\partial x_j}}$. This comparison is presented in Fig. 10. The resolution conditions are shown for both axial and stream-normal directions. As seen, this ratio does not exceed 2 in the entire domain, which is considered sufficient to resolve all dissipation scales of the flow [37].

B. Bulk vibrational energy mixing

The amount of vibrational nonequilibrium triggered by the turbulent mixing is first investigated. The flow bulk vibrational energy e_v is simply computed by adding the vibrational energy across the

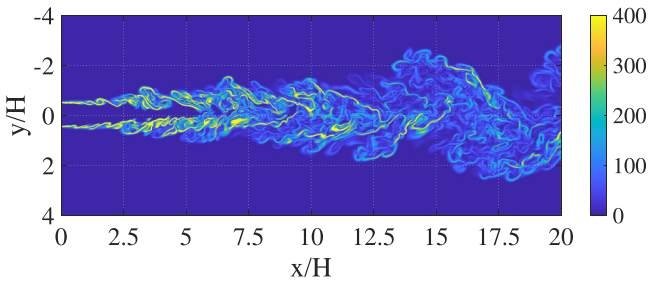

FIG. 9. Snapshots of the magnitude of density gradient in kg/m^4 inside the turbulent planar jet.

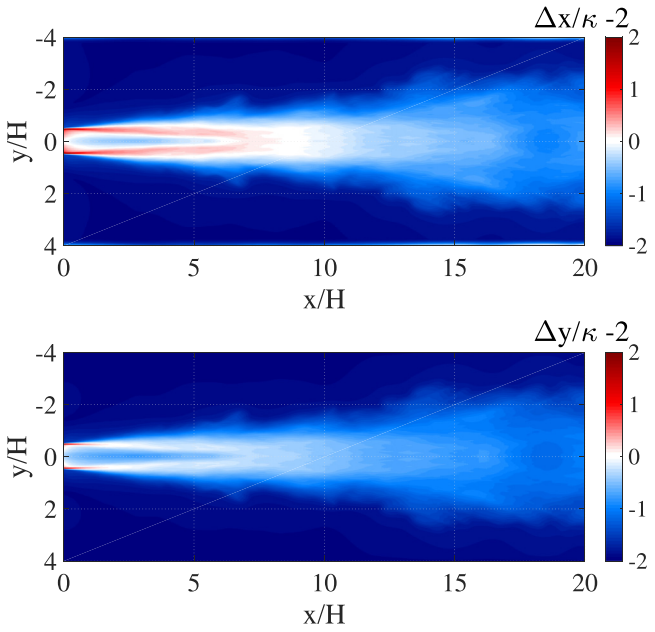

FIG. 10. Spatial resolution in the (top) x and (bottom) y directions.

10 states populations. Its local equilibrated value $e_v{}^*$ is computed from the conservation of energy based on the equilibrated temperature T^*, such that

$$e_v^*(T^*) + c_v T^* = e_v + c_v T. \tag{33}$$

In the above relation, T^* is found using an iterative procedure such that the change in temperature between successive iterations is less than 0.01%.

The normalized relative difference between e_v and e_v^*, defined as $\frac{e_v - e_v^*}{e_v^*} - 1$, quantifies nonequilibrium. It is shown in Fig. 11 as a percentage. The mixing layer is overwhelmingly vibrationally underexcited, with peak departure from equilibrium around 5% from its equilibrated state. Interestingly, some highly turbulent areas exist where the flow is locally vibrationally over-excited. Since the mass entrainment ratio (defined based on Ref. [38]) is equal to unity in the current configuration,

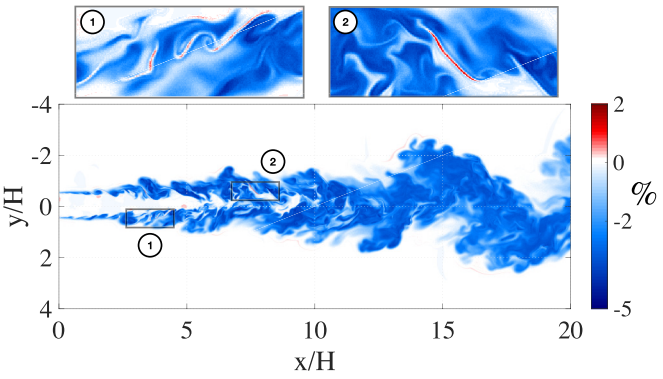

FIG. 11. Snapshots of departure between e_v and $e_v{}^*$ [%]. Red/blue indicate a locally vibrationally over-/under-excited population.

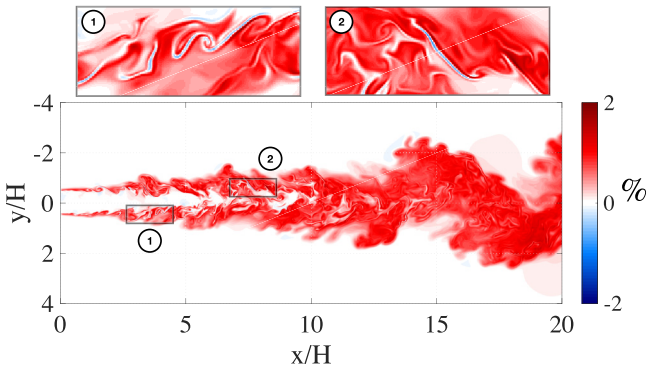

FIG. 12. Snapshot of compressibility factor $\mathcal{C}$ [%]. Red/blue indicate a locally compressed/expanded flow.

both hot and cold fluids mix equally. In such a case, Reising *et al.* [32] predicted that e_v should be symmetrically distributed across the mixing layer. In other words, the inner side, closer to the cold flow, should be vibrationally under-excited, while the outer layer should instead be vibrationally over-excited.

This observation can be explained by considering the source of nonequilibrium. It is seen that the flow is mostly under-excited, implying that T is larger than the implied T_v calculated from e_v. Contrary to the vibrational energy, which changes slowly and only through state transitions, T is coupled to other flow-related variables. In particular, even at subsonic speeds, the exchange of energy between translational and bulk mechanical energy modes is important. Hence, as the jet flow slows down while it interacts with the slower coflow, the local temperature increases very rapidly through compression. This happens at constant Z_{mix} as no mixing is needed to decelerate a flow element emerging from the jet potential core. This implies that compressibility triggers nonequilibrium, in particular, cold nonequilibrium, since e_v remains nearly constant because it relaxes slowly. By the same argument, the acceleration of the outer shear layer should trigger hot nonequilibrium, but is not observed in this configuration. This is explained by considering the volume entrainment rather than the mass entrainment ratio [38]. For the given inflow conditions, this ratio is 2.1, which indicates that the lower-density jet dominates the nonequilibrium generation process. As a result, the mixing layer shows an overwhelmingly cold nonequilibrium driven by compressibility of the fluid.

A compressibility factor $\mathcal{C}$ can be defined in order to locate the regions where such mechanical-translational energy exchange is present. This factor is extracted as the ratio of the local ro-translational energy to the mixing-based expected energy:

$$\mathcal{C} = \frac{c_v T}{c_v[(Z_{\text{mix}} T_{\text{jet}} + (1 - Z_{\text{mix}}) T_{\text{coflow}})]} - 1, \tag{34}$$

where Z_{mix} is the local mixture fraction. $\mathcal{C}$ is plotted in Fig. 12 as a percentage. A positive value indicates that the flow is locally compressed, which should result in cold nonequilibrium. Interestingly, the compressibility plots reproduce the features found in the vibrational energy relative different plots (see Fig. 11). Notably, the rare vibrationally hot areas coincide with the rare expanded areas. This is further quantified in Fig. 13, which presents scatter plots of the relative error between e_v and e_v^* against the mixture fraction and $\mathcal{C}$. The color scheme indicates the number of realizations in a bin (blue is lowest, yellow is highest). The conditional plot against mixture fraction shows that much of the nonequilibrium is vibrationally under-excited, which is essentially the same data represented as in Fig. 11 but represented differently. The relative difference plot against $\mathcal{C}$ clearly shows that much of the nonequilibrium is created when $\mathcal{C} > 0$, which is in regions where compressibility has raised the translational temperature of the fluid. However, the relatively sparse

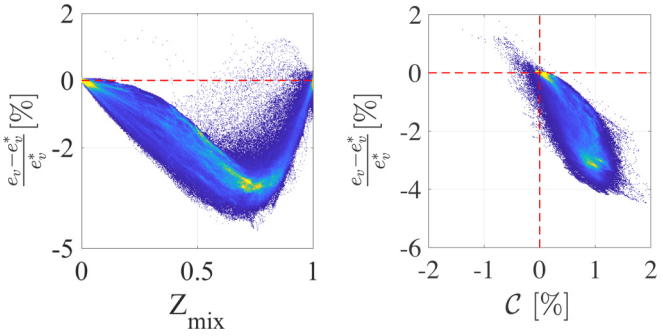

FIG. 13. Scatter plot of relative difference of e_v against the mixture fraction Z_{mix} (left) and the compressibility factor (right) colored by local realization count (blue is lowest, yellow is highest). Plots obtained for case 1.

hot equilibrium is created by the local acceleration or expansion of the fluid, which reduces the translational temperature. Such hot nonequilibrium tend to occur in the close vicinity of the cold jet potential core, where the local mixture fraction is closer to 1.

For the inverse simulations (case 2), the central jet issues at a higher temperature than the coflow and a higher velocity. As a result, the compressibility factor behaves similar to case 1, but shows some differences as well. Figure 14 shows the relative difference in the vibrational energy, which indicates an under-excitation similar to case 1. The compressibility factor also shows a similar behavior (Fig. 15), with positive $\mathcal{C}$ in the mixing layer. However, due to the differences in the density, the mass and volume entrainment ratios are reversed in case 2. As a result, the outer part of the mixing layer shows regions of negative compressibility factor, akin to Reising's theory of symmetric behavior [32].

This effect is further seen in the scatter plots shown in Fig. 16. It is seen that the relative difference of vibrational energy as compared to the equilibrium energy is negative, but is found in regions of negative compressibility as well. Since such regions occur closer to the coflow, which has a lower temperature, it can be inferred that this part of the nonequilibrium is caused purely by mixing between two streams with different temperatures. However, to fully isolate the effect of compressibility, a shearless mixing layer should be used. However, we found that a turbulent mixing region could not be sustained at these conditions without a velocity difference between the streams.

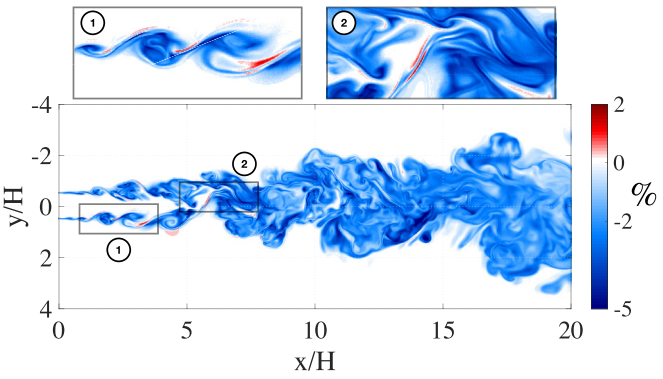

FIG. 14. Snapshots of departure between e_v and $e_v{}^*$ [%] for case 2. Red/blue indicate a locally vibrationally over-/under-excited population.

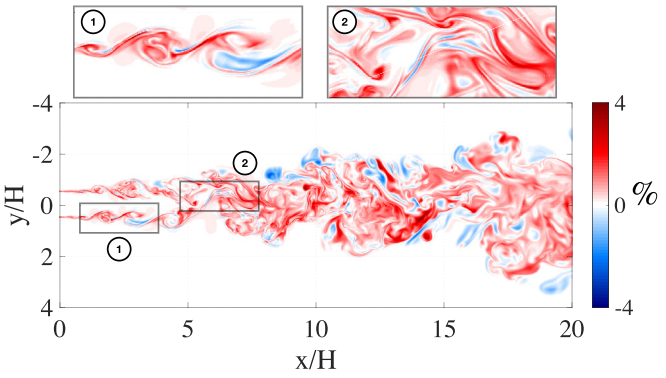

FIG. 15. Snapshot of compressibility factor $\mathcal{C}$ [%] for case 2. Red/blue indicate a locally compressed/expanded flow.

C. Turbulent mixing of vibrational energy states populations

The analysis of the spatial distribution of vibrational energy revealed that the mixing layer is dominated by compressibility, leading to under-excitation of the vibrational population distribution. To further understand the impact of nonequilibrium on the different energy states, instantaneous snapshots of the fractional populations in selected vibrational states are shown for both cases in Fig. 17. It is seen that the mixing patterns are different for the various states. The lower vibrational level exhibits spatial distribution that is consistent with passive scalar mixing: it presents a gradual change from the lower population core jet to the coflow. However, the higher vibrational level exhibits abrupt changes from cold to hot, similar to fast reacting scalars. For the hot jet configuration (case 2), the patterns are simply reversed with an inner jet exhibiting higher population in all the states shown. Note that when the temperature increases, the ground energy level ($v = 0$) loses molecules to higher energy levels.

The differences in the behavior of the different energy levels are more evident in scatter plots against mixture fraction shown in Fig. 18. The data are bounded by two curves: (a) the linear mixing line that provides the limit when state-to-state transitions are frozen, and (b) the equilibrium line that provides the limit when the time to reach a Boltzmann distribution is much faster than any of the timescales associated with the flow. The mixing line is obtained as

$$\phi_v^{\text{mix}} = f_v(v, T_{\text{jet}})Z_{\text{mix}} + f_v(v, T_{\text{coflow}})(1 - Z_{\text{mix}}), \tag{35}$$

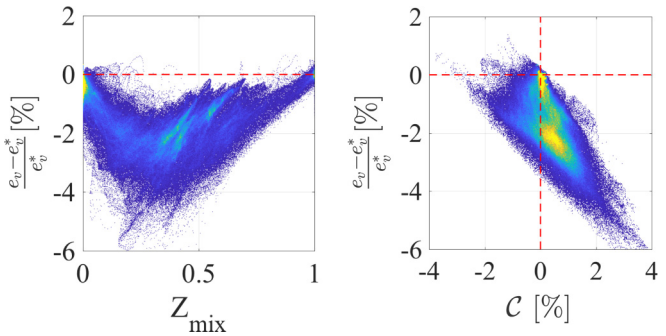

FIG. 16. Scatter plot of relative difference of e_v against the mixture fraction Z_{mix} (left) and the compressibility factor (right) colored by local realization count (blue is lowest, yellow is highest). Plots obtained for case 2.

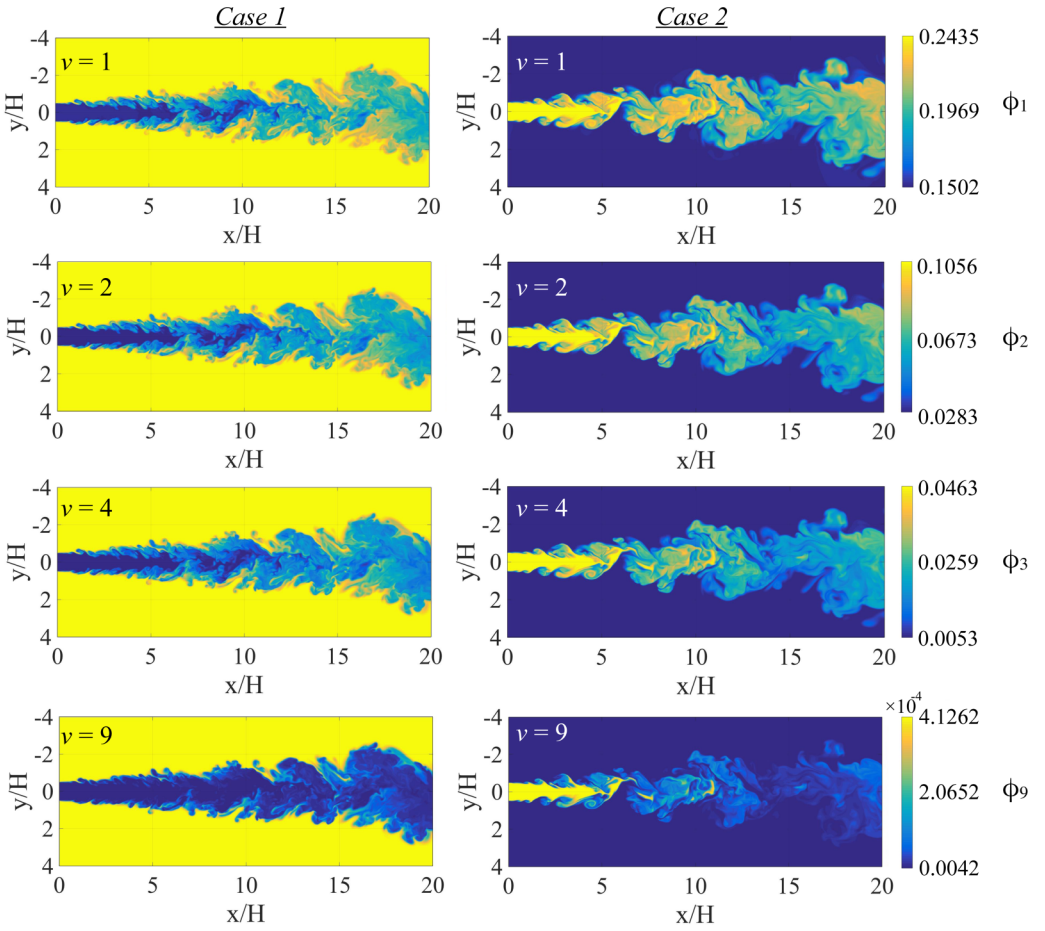

FIG. 17. Snapshots of vibrational state population number densities ϕ_v for levels $v \in [1\ 2\ 4\ 9]$ from top to bottom for the (left) cold jet and (right) hot jet.

while the equilibrium line is simply obtained from the Boltzmann distribution at the equilibrium temperature T^* [Eq. (33)]. The area between the bounding lines increases with the energy level since higher energy level distributions are more sensitive to temperature due to the exponential term in the Boltzmann distribution function. Further, the higher level populations equilibrate rapidly, and all populations above $v = 3$ lie close to the equilibrium line. However, the lower levels relax more slowly, with $v = [0\ 1\ 2]$ populations showing significant scatter away from both limits. Hence, these levels exhibit the highest interaction between state-to-state transition chemistry and turbulence. These plots clearly demonstrate that turbulence can interfere with relaxation both due to compressibility of the flow and the timescales associated with the relaxation process itself.

In the discussions above, it was concluded that the vibrational population is under-excited based on comparison with equilibrium energy. To further understand the distribution of population, the departure of each state from the corresponding Boltzmann fraction can be obtained. To this end, a departure function $\mathcal{E}_v$ is defined as

$$\mathcal{E}_v = \frac{\phi_v - \mathcal{B}_v(e_v)}{\mathcal{B}_v(e_v)}, \tag{36}$$

where $\mathcal{B}_v(e_v)$ is the number fraction of level v for a Boltzmann distribution yielding the same bulk e_v. Figure 19 shows instantaneous snapshots and conditional plots against mixture fraction

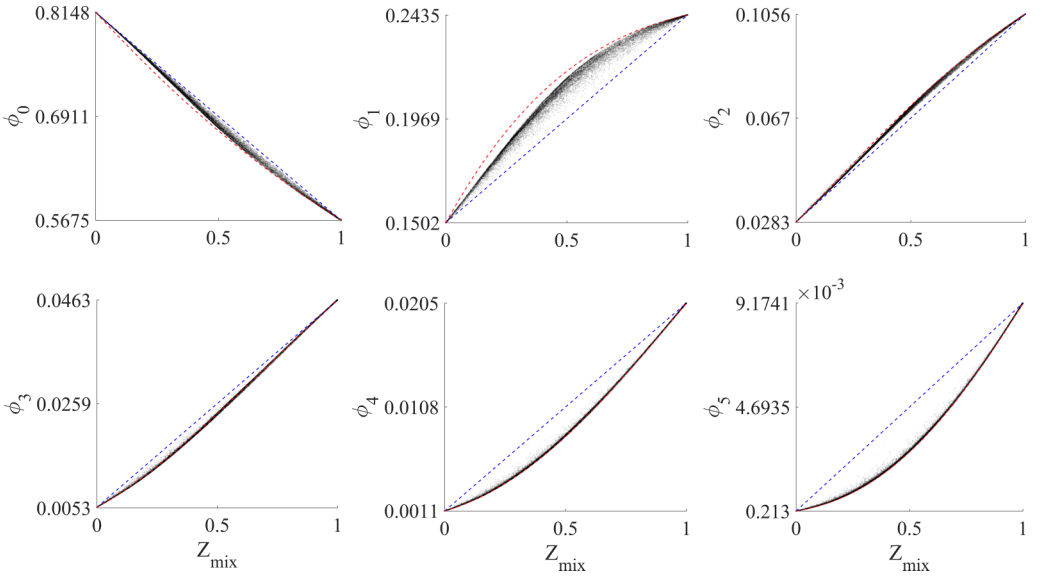

FIG. 18. (Black dots) Distribution of state populations ϕ_v for $v \in [0\ 1\ 2\ 3\ 4\ 5]$ with (dashed blue) $\phi_v(T = 2000K)Z_{\text{mix}} + \phi_v(T = 4000K)(1 - Z_{\text{mix}})$ and (dashed red) the Boltzmann number fractions $f_v(v, T)$. Only case 1 is shown.

of this departure function for select vibrational levels. For $v = 1$, the departure function is always negative, indicating that the population is lower than that observed at equilibrium. This is consistent with the under-excitation of the vibrational energy seen in the discussions above. Since the lower levels contain most of the molecular population, this under-excitation is reflected in the integrated vibrational energy. The higher levels show interesting trends: $v = 3$ and higher levels show significant over-excitation across the mixing layer. Note that the departure function is defined with respect to the local integrated vibrational energy and not the equilibrium energy. The over-excitation of the higher levels indicates that (a) the higher levels are first over-populated compared to equilibrium, (b) the exchange of population between the levels leads to equilibrium. In other words, the translational energy is first transferred into the higher vibrational levels, probably due to the smaller gap in energy. This result has important implications. Since chemical reactions depend preferentially on the higher vibrational levels [10,21], this relaxation route has the potential to alter chemical reaction rates. The integrated vibrational energy itself is dependent on the lower energy levels. As a result, the use of multitemperature models that rely on the local vibrational energy may vastly under-predict the populations in the higher levels.

VI. CONCLUSIONS

The conservation equations of a compressible flow solver resolving vibrational nonequilibrium using a state-specific approach were presented. The QCT method was used to calculate a set of vibrational state-specific scattering rates for the collision $N_2(v_1) + N_2(v_2)$. For the flow conditions considered, the maximum temperature was 6000 K. Hence, only the first ten vibrational states were considered as the population density in higher states is generally very small. During the QCT simulation, the translational-rotational energy was sampled from one of nine temperatures ranging from 500 K to 6000 K. In total, 2.8 billion trajectories were simulated to calculate the set of rates.

An initial test using homogeneous mixing of streams was used to evaluate the state-specific rates. Interestingly, it was found that the mixing process is not linear as implied by the Landau-Teller description of vibrational relaxation but follows a highly nonlinear evolution. In particular,

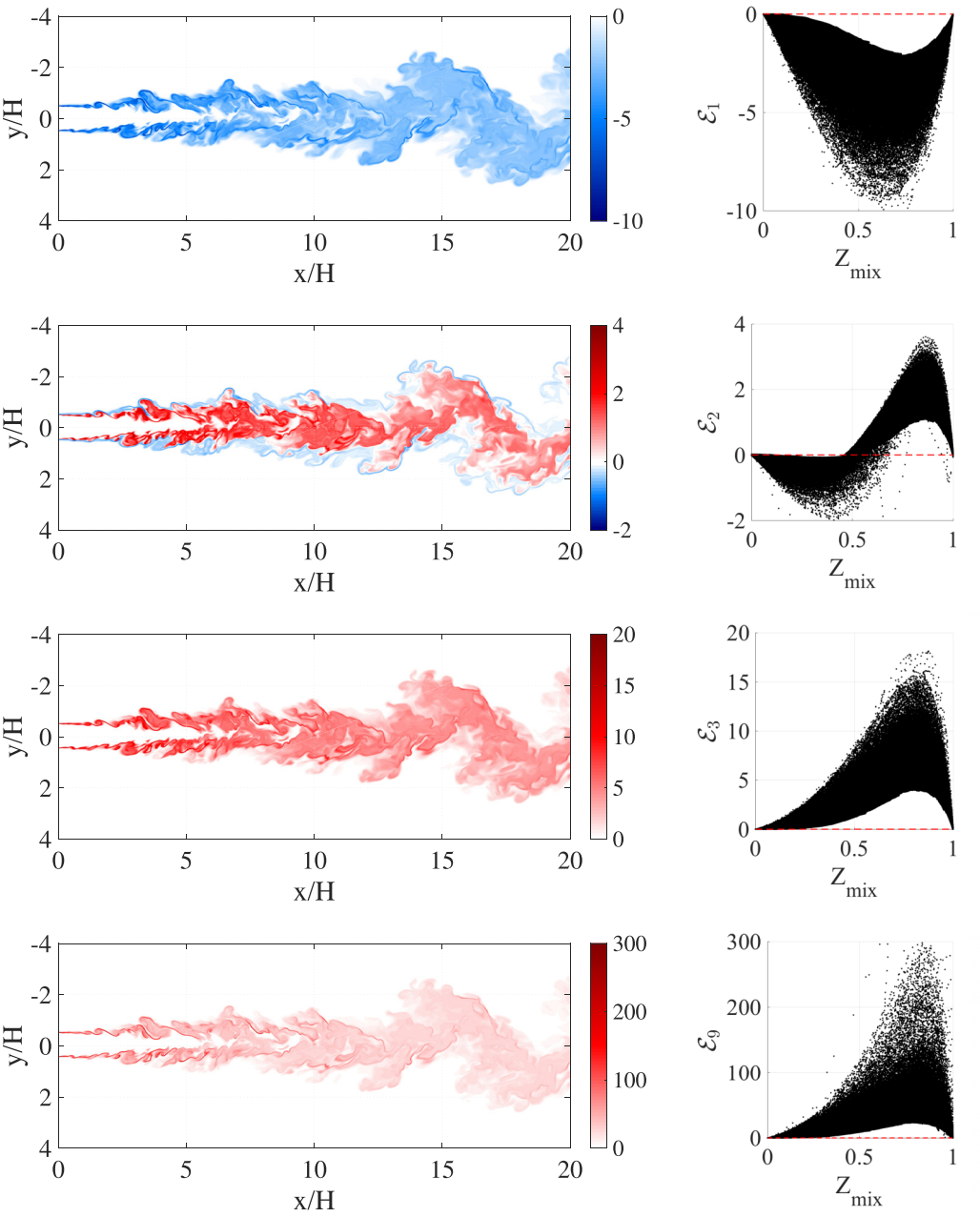

FIG. 19. (Left) Instantaneous snapshots of $\mathcal{E}_v$ [%] for $v \in [1\ 2\ 3\ 9]$ from top to bottom. (Right) Realizations of $\mathcal{E}_v$ [%] for $v \in [1\ 2\ 3\ 9]$ from top to bottom with Z_{mix}.

the high-lying states relax fast, with the lower states relaxing at a much slower rate. This leads to a pseudo-steady behavior, whereby the higher states continuously adjust to the relaxation of the lower states. A relaxation timescale, obtained by tracking the total vibrational energy relaxation towards its equilibrium value, showed trends that are consistent with the Millikan-White correlation, but also showed differences, In particular, the timescale is quantitatively different from that predicted by the experiments, and is dependent on the nature of relaxation. If the initial vibrational temperature

is lower than the translational temperature, the relaxation process was slower than in the inverse scenario. These studies exhibit the complexities of vibrational relaxation, and the need to consider details of the state-specific cross-sections.

Direct numerical simulations of turbulent plane jet coupled with a vibrational state populations solver were then performed to investigate the coupling between turbulence mixing and vibrational nonequilibrium for jet and co-flow temperatures of 2000 and 4000 K. It was found that the nonequilibrium generated at such flow enthalpies are dominated by compressibility effects, where the local acceleration and deceleration of the flow leads to a change in the translational temperature, which then affects the vibrational temperature. This resulted in a non-Boltzmann distribution throughout the mixing layer, which would potentially affect chemical reactions. In particular, a numerical description of nonequilibrium only resolving the bulk vibrational energy, i.e., integrated over the whole energy level distribution, would not be able to resolve such details and would underestimate the reaction rates.

In summary, the use of state-specific rates is important even for internal flows and nominally low translational and vibrational temperatures. Such flows already exhibit significant deviations from Boltzmann distributions, especially for the high-lying states. Since chemical reactions are affected more by the higher energies, any resulting chemical transformation will not follow Boltzmann-based rate expressions. The impact of non-Boltzmann distributions on the macroscopic observed rates needs to be studied in more detail.

ACKNOWLEDGMENTS

This work was supported financially through AFOSR BRI Award No. FA9550-12-1-0460 with Dr. Ivett Leyva as Program Manager. Philip Varghese gratefully acknowledges the support of a Moncrief Fellowship that enabled extended visits to the University of Michigan in Spring 2016. The authors also gratefully acknowledge the generous allocation of computing time by the Texas Advanced Computing Center and NASA High-End Computing (HEC) Program through the NASA Advanced Supercomputing (NAS) Division at Ames Research Center.

[1] I. D. Boyd and T. E. Schwartzentruber, *Nonequilibrium Gas Dynamics and Molecular Simulation*, Cambridge Aerospace Series (Cambridge University Press, Cambridge, 2017).

[2] W. G. Vincenti and C. H. Kruger, *Introduction to Physical Gas Dynamics* (Krieger Publishing Company, Melbourne, FL, USA, 1975).

[3] R. Fiévet and V. Raman, Effect of Vibrational Nonequilibrium on Isolator Shock Structure, J. Propulsion Power **34**, 1334 (2018).

[4] R. Fiévet, S. Voelkel, H. Koo, V. Raman, and P. L. Varghese, Effect of thermal nonequilibrium on ignition in scramjet combustors, Proc. Combust. Inst. **36**, 2901 (2017).

[5] O. Knab, H. H. Fruhauf, and E. W. Messerschmid, Theory and validation of the physically consistent coupled vibration-chemistry-vibration model, J. Thermophys. Heat Transfer **9**, 219 (1995).

[6] A. G. Neville, I. Nompelis, P. K. Subbareddy, and G. V. Candler, Effect of thermal non-equilibrium on decaying isotropic turbulence, in *Proceedings of the 7th AIAA Theoretical Fluid Mechanics Conference, 16–20 June 2014, Atlanta, GA*, AIAA 2014-3204 (2014).

[7] H. Koo, V. Raman, and P. Varghese, Direct numerical simulation of supersonic combustion with thermal nonequilibrium, Proc. Combust. Inst. **35**, 2145 (2015).

[8] A. Viviani and G. Pezzella, Nonequilibrium aerothermodynamics for a capsule reentry vehicle, Eng. Appl. Comput. Fluid Mech. **3**, 543 (2009).

[9] S. Voelkel, V. Raman, and P. L. Varghese, Effect of thermal nonequilibrium on reactions in hydrogen combustion, Shock Waves, 1 (2016).

[10] O. Knab, T. H. Gogel, H. H. Fruhauf, and E. W. Messerschmid, Cvcv-model validation by means of radiative heating calculations, in *Proceedings of the 33rd AIAA Aerospace Science Meeting and Exhibit*, AIAA-95-0623 (1995).

[11] C. Park, Assessment of a two-temperature kinetic model for dissociating and weakly ionizing nitrogen, J. Thermophys. **2**, 8 (1988).

[12] I. V. Arsentiev, B. I. Loukhovitski, and A. M. Starik, Application of state-to-state approach in estimation of thermally nonequilibrium reaction rate constants in mode approximation, Chem. Phys. **398**, 73 (2012).

[13] R. Fiévet, H. Koo, and V. Raman, Numerical simulation of a scramjet isolator with thermodynamic nonequilibrium, in *Proceedings of the 22nd AIAA Computational Fluid Dynamics Conference, 22–26 June 2015, Dallas, TX*, AIAA-2015-3418 (2015).

[14] H. H. Reising, T. W. Haller, N. T. Clemens, P. V. Varghese, R. Fiévet, and V. Raman, Spontaneous raman scattering temperature measurements and large eddy simulations of vibrational non-equilibrium in high-speed jet flames, in *Proceedings of the 32nd AIAA Aerodynamic Measurement Technology and Ground Testing Conference, 13–17 June 2016, Washington, D.C.*, AIAA 2016-3144 (2016).

[15] I. D. Boyd and E. Josyula, Detailed analysis of vibrational nonequilibrium of molecular oxygen in shock-heated flow, Phys. Rev. Fluids **2**, 123401 (2017).

[16] A. Munafo, Y. Liu, and M. Panesi, Modeling of dissociation and energy transfer in shock-heated nitrogen flows, Phys. Fluids **27** (2015).

[17] D. A. Andrienko and I. D. Boyd, High fidelity modeling of thermal relaxation and dissociation of oxygen, Phys. Fluids **27**, 116101 (2015).

[18] R. L. Macdonald, M. S. Grover, T. E. Schwartzentruber, and M. Panesi, Construction of a coarse-grain quasi-classical trajectory method. ii. comparison against the direct molecular simulation method, J. Chem. Phys. **148**, 054310 (2018).

[19] M. Panesi, A. Munafo, T. E. Magin, and R. L. Jaffe, Nonequilibrium shock-heated nitrogen flows using a rovibrational state-to-state method, Phys. Rev. E **90**, 013009 (2014).

[20] J. D. Bender, P. Valentini, I. Nompelis, Y. Paukku, Z. Varga, D. G. Truhlar, T. Schwartzentruber, and G. V. Candler, An improved potential energy surface and multi-temperature quasiclassical trajectory calculations of $N_2 + N_2$ dissociation reactions, J. Chem. Phys. **143**, 054304 (2015).

[21] S. Voelkel, P. L. Varghese, and V. Raman, Multitemperature dissociation rate of $n_2 + n_2 \rightarrow n_2 + n + n$ calculated using selective sampling quasi-classical trajectory analysis, J. Thermophys. Heat Transfer **31**, 965 (2017).

[22] J. I. Steinfeld, J. S. Francisco, and W. L. Hase, *Chemical Reaction Kinetics and Dynamics*, 2nd ed. (Prentice-Hall, New York, NY, 1999).

[23] B. J. Mcbride, S. Gordon, and M. A. Reno, Coefficients for Calculating Thermodynamic and Transport Properties of Individual Species, Tech. Rep. NASA-TM-4513 (NASA Lewis Research Center, Cleveland, OH, 1993).

[24] R. Fiévet,, H. Koo, A. H. Auslender, and V. Raman, Numerical investigation of shock train response to inflow boundary layer variations, AIAA J. **55**, 2888 (2017).

[25] S. Voelkel, P. L. Varghese, and V. Raman, Quasi-state-specific QCT method for calculating the dissociation rate of nitrogen in thermal non-equilibrium, in *Proceedings of the 54th AIAA Aerospace Sciences Meeting, 4-8 January 2016, San Diego, CA*, AIAA 2016-0449 (2016).

[26] S. Voelkel, Thermal Nonequilibrium Models for High-temperature Reactive Processes, Ph.D. thesis, The University of Texas at Austin (2016).

[27] Y. Paukku, K. R. Yang, Z. Varga, and D. G. Truhlar, Global *ab initio* ground-state potential energy surface of N_4, J. Chem. Phys. **139**, 044309 (2013).

[28] R. J. Duchovic, Y. L. Volobuev, G. C. Lynch, A. W. Jasper, D. G. Truhlar, T. C. Allison, A. F. Wagner, B. C. Garrett, J. Espinosa-García, and J. C. Corchado, POTLIB, http://comp.chem.umn.edu/potlib.

[29] P. Valentini, T. E. Schwartzentruber, J. D. Bender, I. Nompelis, and G. V. Candler, Direct molecular simulation of nitrogen dissociation based on an *ab initio* potential energy surface, Phys. Fluids **27**, 086102 (2015).

[30] N. E. Henriksen and F. Y. Hansen, *Theories of Molecular Reaction Dynamics: The Microscopic Foundation of Chemical Kinetics*, Oxford Graduate Texts (Oxford University Press, Oxford, 2012).
[31] R. C. Millikan and D. R. White, Systematics of vibrational relaxation, J. Chem. Phys. **39**, 3209 (1963).
[32] H. H. Reising, Utsav KC, N. T. Clemens, and P. L. Varghese, Measurement of mixing-induced thermal non-equilibrium in a supersonic shear layer using spontaneous Raman scattering, Phys. Fluids **29**, 076101 (2017).
[33] T. J. Poinsot and S. K. Lele, Boundary conditions for direct simulations of compressible viscous flows, J. Comput. Phys. **101**, 104 (1992).
[34] G.-S. Jiang and C.-W. Shu, Efficient implementation of weighted ENO schemes, J. Comput. Phys. **126**, 202 (1996).
[35] H. Koo, Large-Eddy Simulations of Scramjet Engines, Ph.D. thesis, The University of Texas at Austin (2011).
[36] N. Peters, *Turbulent Combustion* (Cambridge University Press, Cambridge, 2000).
[37] S. B Pope, Turbulent flows, Meas. Sci. Technol. **12**, 2020 (2001).
[38] P. E. Dimotakis, Two-dimensional shear-layer entrainment, AIAA J. **24**, 1791 (1986).

Correction: The order of the second and third authors did not follow the original input and has been rearranged.